Supplementary Figures

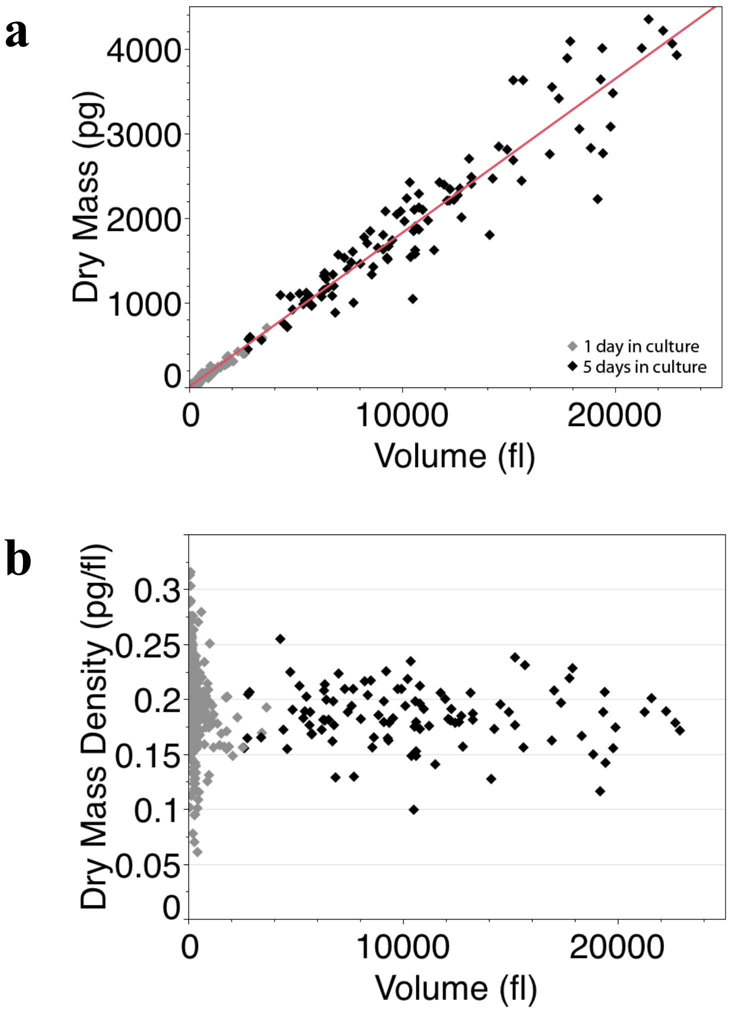

Figure S1: Diffraction phase microscopy measurements of a variety of cell types consistently reflect a "normal" dry mass density for healthy living cells in agreement with the concentration of cytoplasm previously determined by index matching in human oral epithelial cells[17]**.** This includes cells that dramatically increase in volume over their lifetime, for example, the large platelet-producing mouse megakaryocytes that become polyploid and reach volumes up to 25,000 fl without altering their intracellular dry mass density from a value of 0.182 pg/fl. Grey data points represent cells imaged and quantified after one day post-harvest from fetal mouse livers, and black data points represent mature cells after five days in culture. Linear regression slope of 0.182 in (**a**) is equal to the average dry mass density (R^2= 0.872 for cells over 5000 fl).

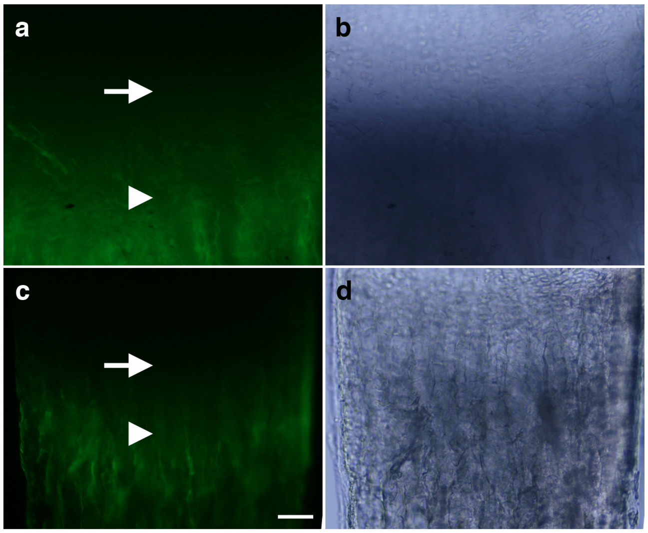

Figure S2: The mouse proximal tibia growth plate elongates at a daily rate approximately 1.55 times faster than the distal metatarsal. a, c, The distance between the oxytetracycline fluorescence (arrowhead) and the edge of the bone trabeculae (arrow) 24 hours after intraperitoneal injection into P5 mice indicates the amount of linear growth per day. **b, d,** DIC images of bisected elements. The average daily growth rate for the mouse proximal tibia growth plate (**a, b**) is 158 µm ± 24.1 compared to 102 µm ± 14.5 for the metatarsal (**c, d**). n=3 animals. Scalebar equals 50 µm.

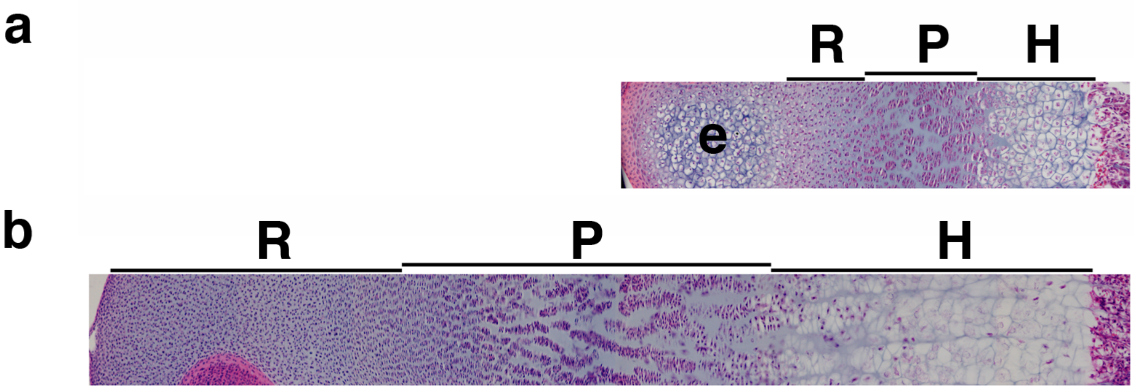

Figure S3: The jerboa distal metatarsal growth plate (b) is proportionately approximately three-times taller in each zone compared to the mouse metatarsal (a). Postnatal day 7 histology by H&E. Joint surface to the left, primary ossification to the right. R, resting zone; P, proliferating zone; H, hypertrophic zone. “e” in panel (**a**) denotes hypertrophic chondrocytes of the forming epiphysis in the mouse that has not yet formed in the age-matched jerboa.

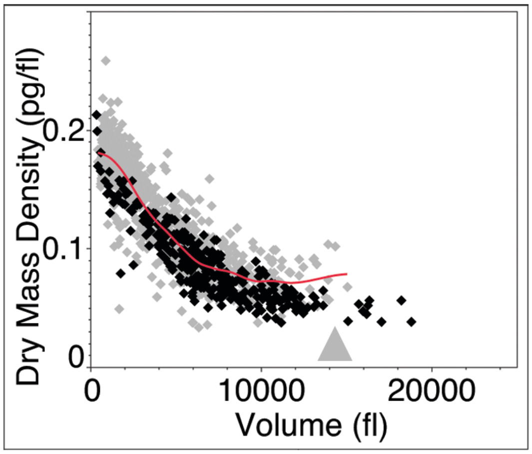

Figure S4: Tibia hypertrophic chondrocytes are slightly larger in the jerboa than in mouse. Dissociated P5 jerboa tibia chondrocytes (black; n=319 cells) achieve sizes slightly larger than mouse (grey, data from Fig. 1) by extending Phase 3.

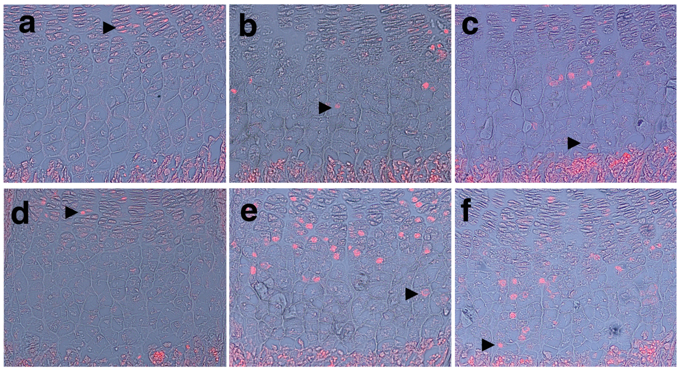

Figure S5: Mouse proximal tibia and distal metatarsal hypertrophic chondrocytes rapidly increase in average cell height. BrDU labeled cells (red) overlayed with the DIC image of the hypertrophic zone indicating the position (arrowhead) of the most distal (bottom of the image) and therefore oldest labeled cell in the mouse P5 proximal tibia (**a, b, c**) and distal metatarsal (**d**, **e**, **f**) at 18h (**a, d**), 30h (**b, e**) and 42h (**c, f**) post BrDU injection.

Supplementary Methods

Animals

CD-1 was chosen as the wild type mouse strain for this study. *Igf1*^{tm1Dlr} conditional mice[21] and *HoxB6-Cre* transgenic mice[22] were previously described. Jerboas were housed and reared as previously described[24]. All animal protocols were approved by the Harvard Medical Area Standing Committee on Animals.

Sectioning and histology

Dissected skeletal elements were fixed overnight at 4°C in 4% paraformaldehyde and then carried through a graded series of ethanol dehydration washes before transition through xylenes and into paraffin wax. Sections were cut at 10-12 μm thickness and stained with hematoxylin and eosine. Average maximum cell heights were measured in the axis of linear growth through the lacunae surrounding the largest cells with a clear nuclear profile from digital images of the hypertrophic zone and averaged across at least 4 sections from at least 3 individuals. Bromodeoxyuridine (100 mg/kg) or oxytetracycline hydrochloride (20 mg/kg) was injected into the peritoneum of postnatal day 5 mice before harvest. BrdU was detected using a rat anti BrdU (AbD Serotech) followed by goat anti-rat Alexa594 (Invitrogen) in paraffin sections. Oxytetracycline was detected by fluorescence in bisected skeletal elements.

Chondrocyte and megakaryocyte isolation

Postnatal day 5 animals were chosen for this study because the tibia and metatarsal growth plates are rapidly elongating in both species, but the metatarsal epiphysis (secondary ossification center) has not yet formed. While the epiphysis of the metatarsal forms by P7 in the mouse, it appears later in the jerboa (Fig. S3). Since the hypertrophic chondrocytes reside in a small domain nearest the chondro-osseous junction, we enriched for these cells by using a razor blade to remove a majority of the cartilage containing resting and proliferative chondrocytes leaving the cells closest to the chondro-osseous junction and a small amount of the adjacent trabecular bone. Growth plates were bisected longitudinally and incubated for 45 minutes at 37°C in 2 mg/ml Collagenase D (Roche) in DMEM/F12 (Invitrogen, 290-330 mOsm) plus 10% fetal calf serum. After the initial incubation, the bone collar, trabecular bone, and loosened connective tissues were manually removed with forceps, and the remaining cartilage fragments were transferred to a fresh dish of collagenase digestion media. Cells were incubated for an additional 2-3 hours with occasional swirling until cells mostly dissociated from the surrounding matrix. Dissociated chondrocytes were transferred to 35 mm dishes with a 14 mm diameter, 1.5-thickness glass bottom (MatTek) and imaged immediately. The largest hypertrophic chondrocytes are a small population of the most mature cells, therefore we further enriched for this population in our data analysis by scanning for fields of view containing the largest cells in the dish and quantified all of the intact spherical neighbors.

There has been a longstanding discussion in the literature regarding the extracellular osmolarity of chondrocytes, primarily in the articular cartilage[9,10,25,26]. Much of this data is based on the theoretical ionic environment in association with charged glycosaminoglycans according to the Donnan-Gibbs equilibrium, though to our knowledge the extracellular osmolarity of growth plate cartilage has not been directly measured. While serum osmolarity is approximately 280 mOsm, the osmolarity in association with cartilage may be upwards of 400 mOsm. To address the possibility that the swelling we observe in chondrocytes at larger volumes may be the response to media of low osmolarity, we repeated the diffraction phase microscopy measurements in mouse proximal tibia growth plates dissociated in 424 mOsm DMEM/F12 raised with sucrose. Media osmolarity was measured using the Vapro Model 5600 (Wescor, Inc). We find the same three phases, including the phase of cell swelling, indicating this is an inherent property of growth plate chondrocytes and not the passive response to an abnormal osmotic environment (Fig. S6). We presume that the 4 hours from dissection to imaging is enough time for volume regulatory mechanisms to compensate for any response to osmotic stress that may have occurred. Indeed, 4-D confocal imaging of in situ porcine articular chondrocytes after osmotic stress shows a mean recovery rate of 4.1%±1.8%/min with 96% volume recovery after about 12 minutes[27].

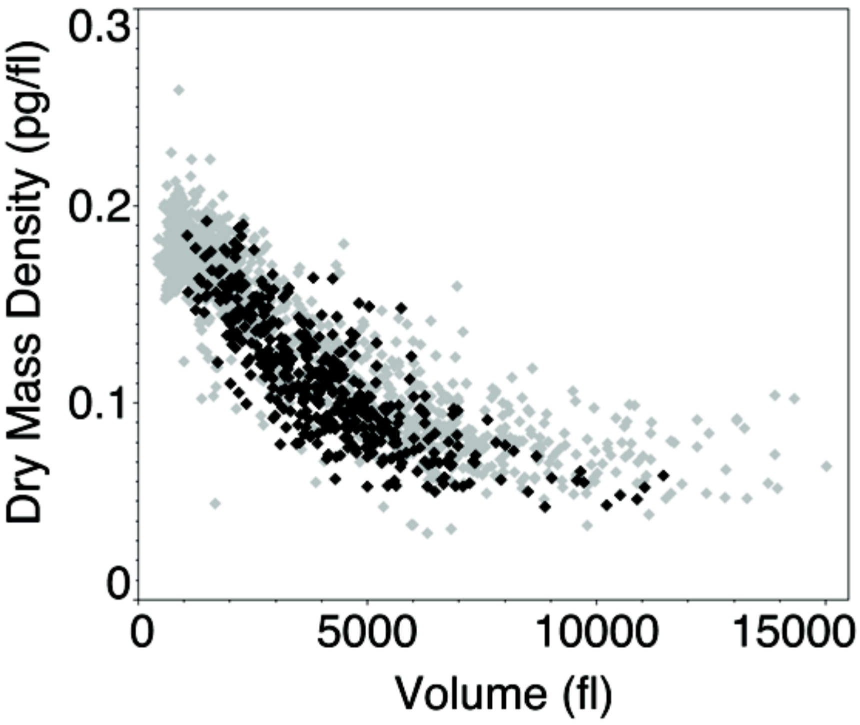

Figure S6: Cell swelling is not the result of low media osmolarity. Diffraction phase microscopy was performed on P5 mouse proximal tibia chondrocytes dissociated in DMEM/F12 raised from 311 to 424 mOsm with sucrose. The high osmolarity cells (black; n=414) follow the same dilution trend as cells dissociated in lower osmolarity media (grey).

Fetal megakaryocytes were isolated from embryonic day 14.5 mouse livers according to previously published protocols[28,29] or generously donated by Dr. Annouck Luyten and Dr. Ramesh Shivdasani. Cells were imaged by DPM one day after harvest or at maturity after five days in culture.

Principle of dry mass measurement using diffraction phase microscopy

The principle of measuring dry mass using diffraction phase microscopy (DPM) can be broken down into two steps. The first part is the principle common to any quantitative phase microscopy[30,31] also known as digital holographic microscopy[32,33]. First, the cells induce a phase shift in the plane wave light that passes through them, and the magnitude of the phase shift is the product of the refractive index and the height. (Fig. S7a) More accurately, the phase retardation

φ is expressed as the integral of the refractive index distribution of the cell $n(x, y, z)$ along the axis of light propagation where n_0 is the refractive index of the media and λ is the wavelength of the light in a vacuum[34].

$$\varphi = \frac{2\pi}{\lambda} \int n(x, y, z) - n_0 dz \qquad \text{(Eq. 1)}$$

We consider the cell as a solution of biological molecules (protein, carbohydrates, nucleic acids etc.) in saline water, where the refractive index of the cell relative to that of media is expressed by a linear equation[12]:

$$n(x, y, z) - n_0 = \frac{dn}{dc} c(x, y, z) \qquad \text{(Eq. 2)}$$

The specific refractive index increment $\frac{dn}{dc}$ is the increment of refractive index change per one percent increase of solute concentration. The values of specific refractive index increment fall in a narrow range for a wide variety of organic substances present in living cells[35]. For human proteins the predicted distribution of the specific refractive increment is close to Gaussian distribution with a mean of 0.190 ml/g and a standard deviation of 0.003 ml/g[36]. Carbohydrates and lipids have lower values ranging in 0.14-0.15 ml/g, and pigments may give rise to unusual refractive index at the absorption bands. Note that as long as the cell's composition ratio of protein, carbohydrate, and lipids stays constant, the choice of the value of $\frac{dn}{dc}$ affects only the multiplicative constant in the calculation of dry mass. We use 0.18 ml/g as the representative refractive increment for typical cytoplasmic material[35].

Combining Eq. 1 and Eq. 2, we obtain the dry mass density per area.

$$\int c(x, y, z) dz = \frac{\lambda}{2\pi} \frac{dc}{dn} \varphi(x, y) \qquad \text{(Eq. 3)}$$

This is integrated over the area of a cell to calculate the cell's dry mass M.

$$M = \iiint c(x, y, z)dxdydz = \frac{\lambda}{2\pi}\frac{dc}{dn}\iint \varphi(x, y)dxdy \qquad \text{(Eq. 4)}$$

The second part is to measure the wave front of light that traversed the sample to obtain $\varphi(x, y)$. The wave front sensing can be achieved in various ways including by interfering the sample field with a plane wave reference field. To be able to calculate the phase from the interference pattern, we employed spatial phase shifting[37]. Spatial phase shifting introduces a fixed angle tilt between the sample and reference fields so that the interference term is shifted in spatial frequency (Fig. S7b and c). This appears as a regular fringe pattern in the interferogram. The interference pattern is expressed as $I(x, y) = I_S + I_R + I_x$ where the interference term I_x is

$$I_x = 2\sqrt{I_S I_R}\cos[\ \varphi + k_0 \cdot x] \qquad \text{(Eq. 5)}$$

and sample field intensity I_S, reference field intensity I_R, and the wave number of the tilt k_0. Since the reference field is a plane wave, the difference of the phase of the sample and reference field is the sum of the phase shift induced by the cell φ, the known tilt $k_0 \cdot x$, and a constant number that represent the optical path length difference between the sample and reference light path which is not relevant in this context.

A 2-dimensional Fourier transform of the interference pattern $\mathcal{F}[I(x, y)](k)$ contains the Fourier transform of Eq. 5, which is as the following.

$$\mathcal{F}[I_x](\mathrm{k}) = \mathcal{F}\left[\sqrt{I_S I_R}\mathrm{e}^{i\varphi}\right](k - k_0) + \mathcal{F}\left[\sqrt{I_S I_R}\mathrm{e}^{-i\varphi}\right](k + k_0) \qquad \text{(Eq. 6)}$$

Note that each term is located around $\pm k_0$ in the Fourier plane. By choosing large enough k_0, these can be spatially separated from the Fourier transform of the non-interferometric terms $\mathcal{F}[I_S + I_R]$. This is equivalent to having more than two fringes in a resolution-limited spot in the image plane. The argument of the inverse Fourier transform of any one term of the right hand side of Eq. 6 yields the desired phase shift $\varphi(x, y)$.

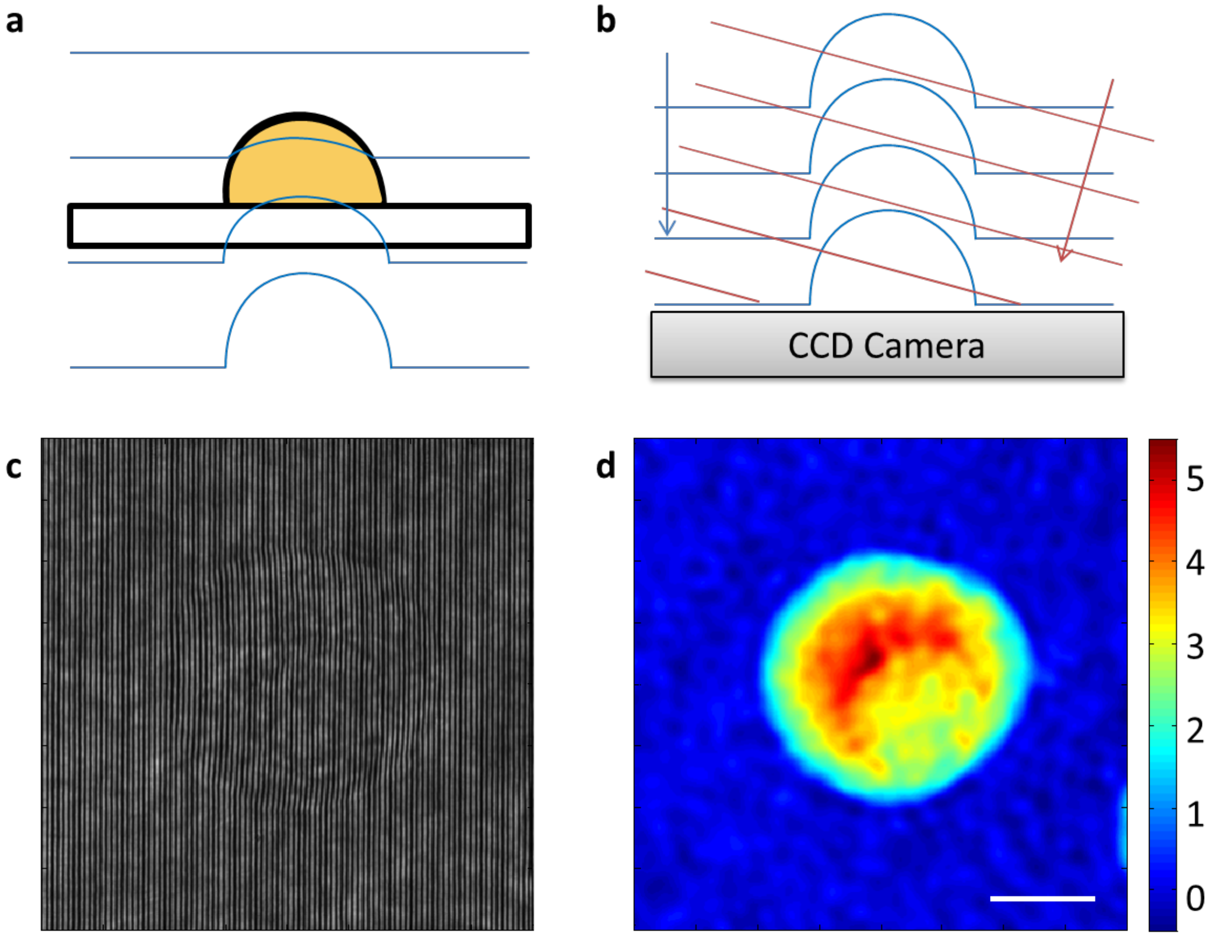

Figure S7: Principle of diffraction phase microscopy. a, The wave front of a plane wave light field is retarded by an amount that is the integral of the refractive index of the cell along the axis of light propagation. When the refractive index is constant, the phase shift is linearly related to the height of the cell. **b,** In the spatial phase shifting technique, the reference field (red) is combined with the sample field (blue) at a fixed angle. The interference pattern is recorded using a CCD camera and used to calculate the phase shift of the sample field. **c,** Interference pattern recorded by the camera. **d,** The phase shift calculated from (**c**). Colorbar is in radians. Scale bar is 10 μm.

Design of the low coherence diffraction phase microscope

To apply quantitative phase microscopy to the study of hypertrophic chondrocytes, we adapted the previously reported diffraction phase microscope design[16,38]. The quantitative phase image from a diffraction phase microscope (DPM) can be obtained from a single interferogram. The optical path length of the reference arm and the sample arm is matched by design allowing the use of a low coherence light source such as a superluminescent diode. The coherence length is selected so that the coherence window is sufficiently wide for the sensing of phase shift introduced by cells but short enough to minimize the speckle noise. The design of the diffraction phase microscope is discussed in a previous paper[16]. The unique aspect of this quantitative phase microscope is that it generates the reference plane wave field from the sample field using a 4-f lens pair system in which a diffraction grating is located at the first image plane, and a pinhole and aperture are located at the Fourier plane. The sample field is split into closely directed beams using a diffraction beam splitter (denoted by G in Fig. S8). The zeroth order diffraction beam is focused through a pinhole and becomes a gaussian beam, which is collimated by the second relay lens. A first order diffraction beam passes through an aperture and is imaged on the camera by the same pair of lenses. When the zeroth and first order diffraction beams meet in the second image plane where the camera is located, they converge at an angle determined by the grating's diffraction angle and the magnification of the 4-f lens pair. This tilt angle serves the purpose of spatial phase shifting.

The specification of the DPM used in this study is as follows. The light source is either superluminescent diode (Superlum) with the center wavelength at 830 nm and bandwidth 19.2 nm or a solid state laser (Crystalaser) with the wavelength at 639.8 nm. The magnification of the objective lens is 20x but the image was further magnified by 1.4 - 4x using the relay lens pair to match the pixel size of the CCD camera. Grating pitch was 72 - 120 lines per mm and pinhole size was 8-25 µm depending on the particular combination of the relay lens pair and the camera.

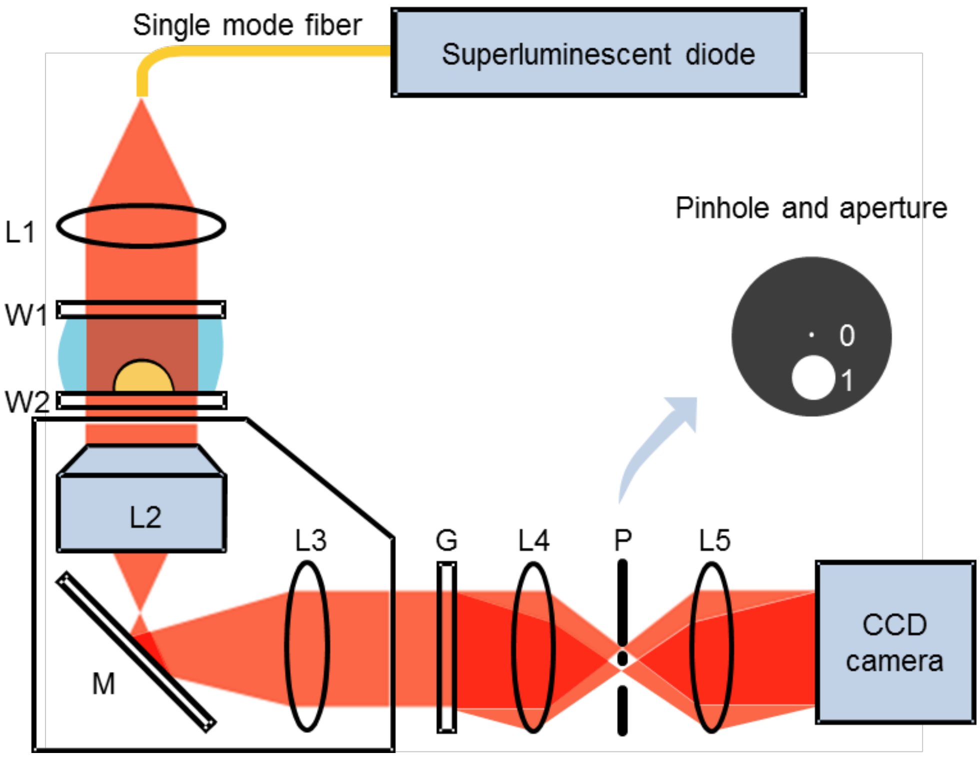

Figure S8: Layout of the diffraction phase microscope. L1, collimation lens. W1 and W2, cover glass. L2, objective lens. L3, tube lens. L4 and L5 relay lenses. M, mirror. G, diffraction grating. P, pinhole and aperture.

Dry mass measurement sensitivity

To demonstrate the measurement sensitivity of dry mass density, we applied the same analysis process on empty areas between cells. A circular region of interest (ROI) was selected and its ‘mass’ was calculated from the quantitative phase shift within the region of interest. The ‘volume’ is calculated from the diameter of ROI assuming a hypothetical spherical object. The fluctuations of phase due to noise contribute to deviation of the ‘mass’ from zero. The ‘dry mass density’ is the ‘mass’ divided by the ‘volume’. Fig. S9 shows the ‘dry mass density’ calculated from the hypothetical spheres of the background area in comparison to those from the cells in the same data set. As expected, the background’s dry mass density value is near zero and the density of cells at the most diluted state is much higher than that of the background.

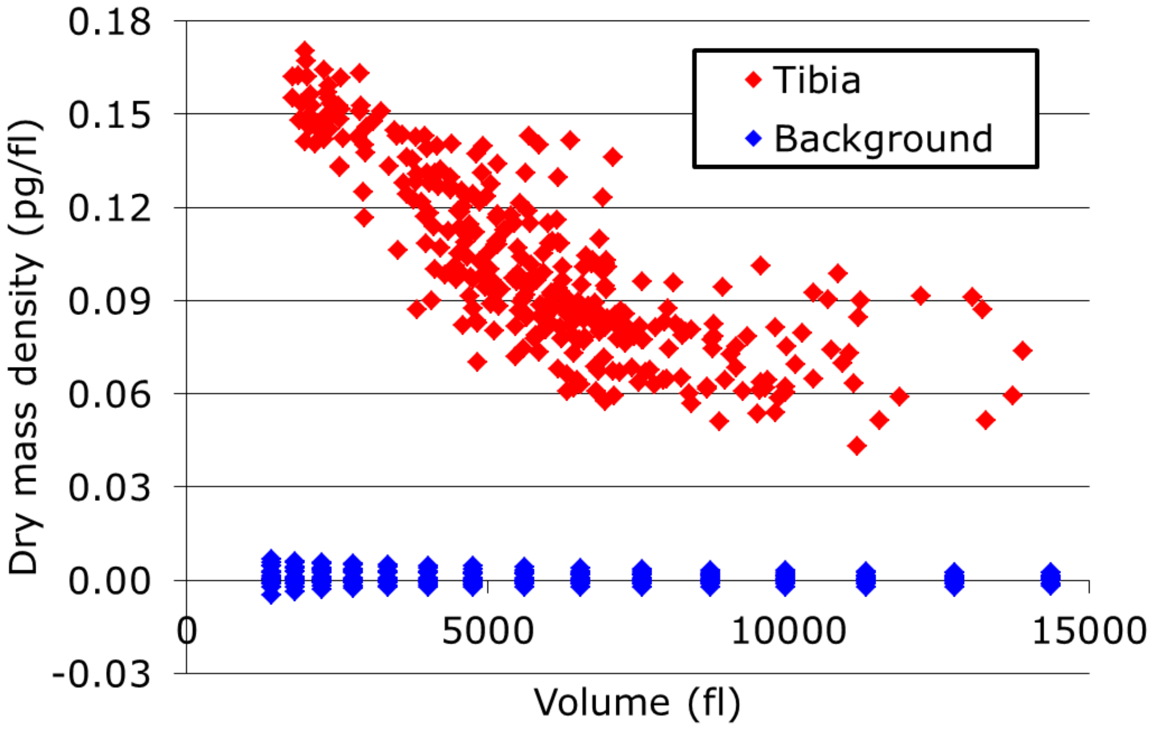

Figure S9: Dry mass density from mouse tibia cells (red) and from the background (blue).

Accuracy of dry mass measurement: Depth of focus of diffraction phase microscope

Fig. S7a illustrates that we operate in the realm of projection approximation, which in practice requires that the illumination beam is a collimated plane wave and that the contribution of scattered light is relatively small compared to the unscattered light. When the projection approximation holds, the entire height of the cell is inside the interval of the z-axis integral in Eq. 4, and therefore the dry mass M obtained from Eq. 4 is equal to the total dry mass of a cell. It is worth noting that the z interval of integration is far greater than the depth of focus of a bright field microscope that uses the same objective lens. While the depth of focus of a 20x 0.75 NA objective lens is only a few microns, the depth of focus (z integration interval) of the diffraction phase microscope is greater than the largest cells we imaged (35 μm).

To demonstrate this, we imaged polystyrene beads that are 5-45 μm in diameter. The refractive index difference of the beads and the immersion oil was chosen to mimic the refractive index contrast of cells in water (0.03). As shown in Fig. S10a, the height of beads calculated from the quantitative phase image agrees with the diameter of the beads. The refractive index of beads relative to the immersion oil can be calculated by dividing the areal integral of phase with the volume calculated from the diameter just like the calculation of dry mass density of spherical cells. Fig. S10b shows that the refractive index of the beads is constant regardless of their size. This demonstrates that the depth of focus of the diffraction phase microscope is greater than 45 μm, and therefore the decrease in dry mass density of large cells is not caused by an optical sectioning artifact.

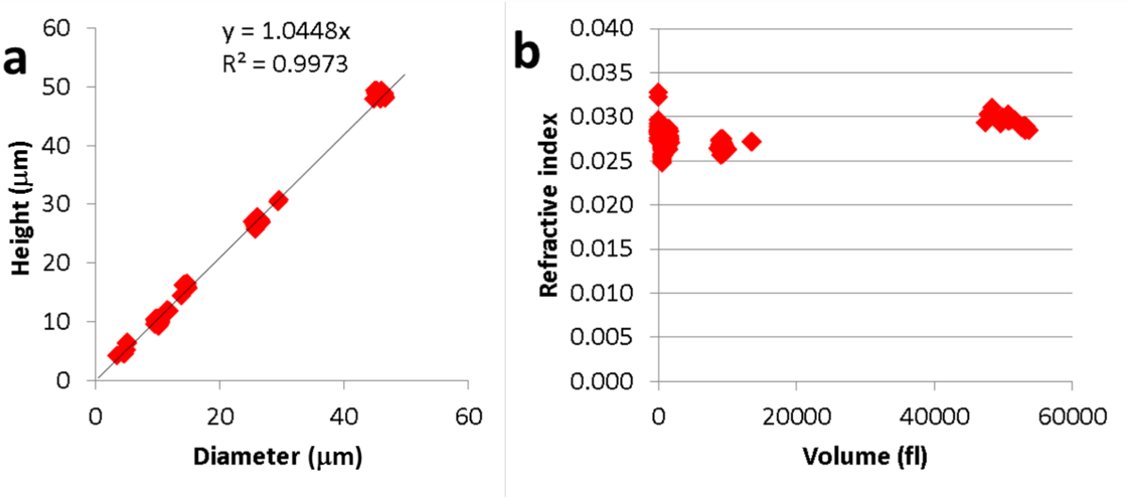

Figure S10: Depth of focus of the diffraction phase microscope is greater than 45 microns. **a,** The height calculated from the quantitative phase image agrees with the diameter. **b**, The refractive index of beads calculated from the quantitative phase and the diameter is constant.

Volume measurement and confirmation of dry mass density reduction

Diffraction phase micropscopy allows us to quantify the dry mass of large numbers of non-adherent chondrocytes but does not directly provide volume information. In this section we provide evidence that the dissociated chondrocytes are spherical, justifying the calculation of the volume from the diameter. Three-dimensional confocal morphometry and refractive index contrast method show that the cells are spherical for all sizes. Additionally, we provide evidence from a third method, regularized tomographic phase microscopy, that allows us to directly measure the dry mass density of a cell without relying on measuring the mass, shape or volume.

The tomographic density measurement supports our findings that hypertrophic chondrocytes enlarge through a multiphase process that includes a phase of cell swelling.

Volume calculation from diameter

For each cell imaged using DPM, the cell's volume was calculated as the volume of a perfect sphere. The diameter of the sphere is determined from the cell's area in the quantitative phase image. We find that the optical diffraction of light around the boundary of a cell or any object makes the boundary detection uncertain by 1.2 pixels or 0.26 μm on average. (Fig. S11). If the object is a 10 μm diameter perfect sphere, this boundary uncertainty corresponds to a 5.2% uncertainty of radius, and thus, 16% uncertainty in volume. This is not stochastic but a systematic error and has the following characteristics: (1) The percentage error decreases with the size of the object. For example, it will be 5% uncertainty in volume for 30 μm diameter sphere. (2) Depending on the threshold for the image segmentation, the result may be close to the true volume. However, usually it is not possible to know the threshold value that achieves perfect image segmentation. Also, it should be noted that the inaccuracy of the boundary detection does not affect the dry mass detection. The phase on the boundary is already close to zero and the contribution from the uncertain area to the total phase integral is less than 0.2%. Rather, the boundary inaccuracy affects the calculated volume of the sphere and thus the dry mass density. Though this uncertainty affects determination of the absolute values of dry mass density, this ambiguity does not affect the observation of the three phases of dry mass density dilution as we apply thresholding consistently throughout the data sets.

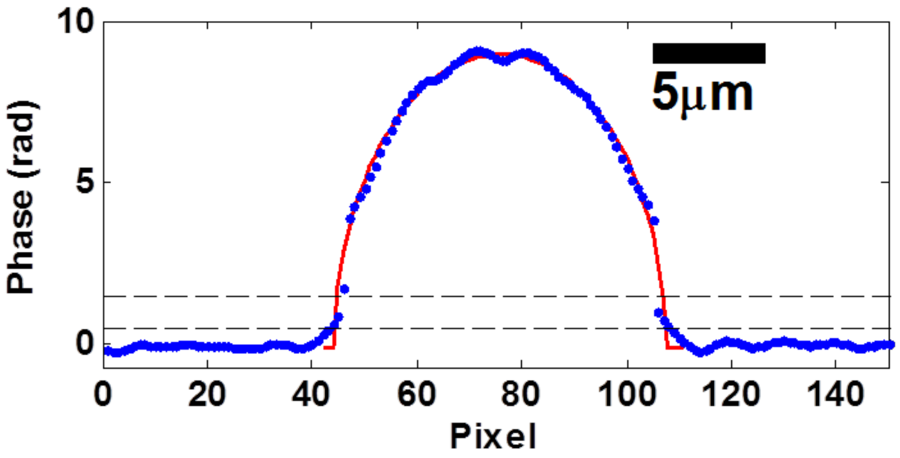

Figure S11: Threshold value for the image segmentation affects the volume calculation. Cross section across the center of a 15 μm borosilicate bead in n=1.66 oil. Blue dots show data from each image pixel. Red line is curve fitting of the data point over 2 radians to a hemicircle model. The boundary of the bead can be limited to between the black dashed lines marking 0.5 and 1.5 radians. Depending on the threshold value, one or two pixels on the boundary may get included to or excluded from the bead.

Three-dimensional confocal morphometry

For three-dimensional confocal morphometry, we labeled the cell boundary using the plasma membrane stain CellMask Orange (Invitrogen C10045) (5 μg/ml in DMEM/F12). Images were acquired by a spinning disk confocal microscope (Yokagawa CSU-X1 on Nikon Ti inverted microscope) equipped with a 60x Plan Apo NA 1.2 water immersion objective lens. Spatial resolution in the x-y plane was 0.1061μm. Z-series optical sections were collected with a step size of 0.2 μm. The use of a water, rather than oil, immersion objective lens ensures that the z-distance of the objective stepping motor translates to the same distance in the sample space where the cells are immersed in media[39]. The acquired z-series were plotted using Matlab without deconvolution or other adjustments.

The plasma membrane stain clearly shows the outer boundary of the cell (Fig. S12a). The height and diameter of a cell are determined by measuring the distance between outermost local intensity maxima in the x-y and x-z cross sections through the center of the cell. The diameter of imaged cells ranged from 20 to 34 μm. The sphericity was quantified by the aspect ratio of the height and diameter (Fig. S12). The average aspect ratio was 1.00 ± 0.010 (Standard error of the mean, N=14) confirming that dissociated hypertrophic chondrocytes are indeed spherical even as they increase in size. The standard deviation of the aspect ratio is 0.04 ± 0.008 (Standard error of the standard deviation) implies that the error in the volume calculation from the diameter is less than 4.8%.

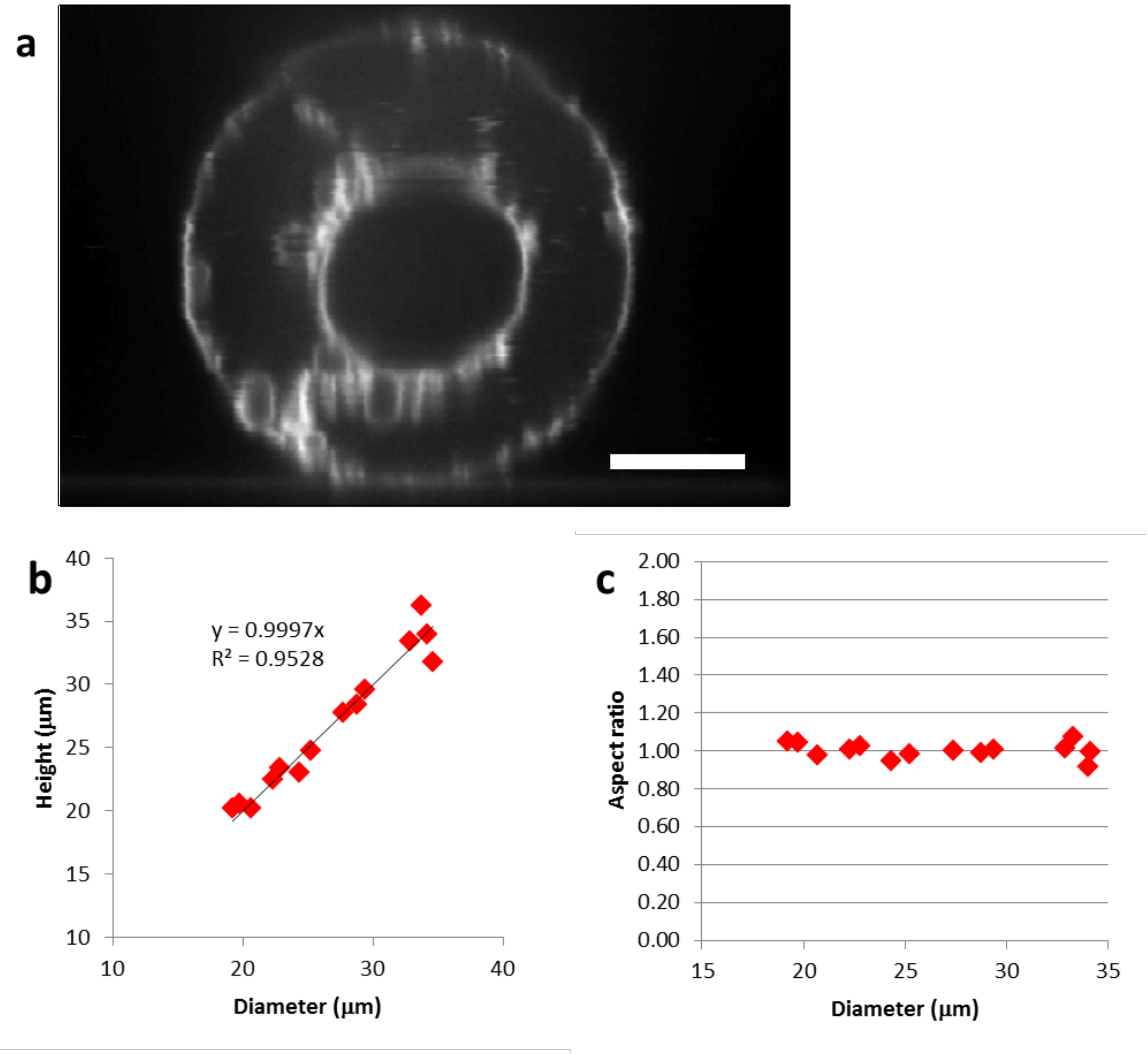

Figure S12: 3D confocal morphometry shows that dissociated hypertrophic chondrocytes are spherical. a, x-z cross section of a dissociated hypertrophic chondrocyte stained with CellMask Orange. Scale bar is 10 microns and applies to both the horizontal and vertical axes. **b**, Diameter and height of dissociated hypertrophic chondrocytes. **c**, The ratio of height and diameter is close to 1 for the measured range of diameters.

Refractive index contrast method

The volume of a live cell can also be measured using quantitative phase microscopy by introducing a contrast agent in the culture media that increases the media's refractive index[17]. Suppose that the additive material is dissolved in the media but not permeable to the cell membrane. The refractive index of the media increases from n_1 to n_2, but the refractive index of the cell $n(x,y)$ remains the same. The integral of the quantitative phase over the area of the cell is $\Phi_j = \int \varphi_j dxdy = \frac{2\pi}{\lambda} \iiint n(x,y) - n_j dxdydz$ for before ($j = 1$) and after ($j = 2$) the addition of the refractive index increasing agent. If the two phase images are taken in a short time it is safe to assume that the cell's dry mass has not changed. This means that the contribution from the cell's refractive index will cancel out in the subtraction of the phase integrals, resulting in $\Phi_1 - \Phi_2 = \frac{2\pi}{\lambda} \iiint n_2 - n_1 dxdydz$. Since a three dimensional integral of a constant over the area and height of the cell is the volume of the cell,

$$\mathrm{V} = \frac{\lambda}{2\pi} \frac{\Phi_1 - \Phi_2}{n_2 - n_1} \qquad \text{(Eq. 7)}$$

We tested this method using borosilicate glass microspheres (Diameter 15.9μm ± 0.6μm, σ = 1.8μm, 11% CV, Thermo Scientific) in immersion oils of different refractive indices (n=1.46 and 1.66 at 593 nm and 25°C, Cargille Labs). Instead of measuring the same bead twice in both oils, we measured multiple beads in each oil and calculated the phase integral Φ_j by interpolation. We detected the boundary of the beads by thresholding at 0.5, 1.0 or 1.5 radians (Fig. S11). The interpolated phase integrals of a 15 μm bead were 1409.1 ± 46.3 rad· μm^2 in n=1.46 oil and -1271.8 ± 75.4 rad· μm^2 in n=1.66 oil, hence, $\Phi_1 - \Phi_2$ is 2680.9 ± 121.7 rad· μm^2. The refractive indices of immersion oils at our applied wavelength of 830 nm are estimated by Cauchy's equation using the refractive index at 486.1, 589.3, and 656.3 nm provided by the manufacturer. The index at 830 nm and 25°C was n_1=1.4542 ± 0.0039 and n_2=1.6388 ± 0.0039 respectively. Hence, the bead volume estimated using Eq. 7 is 1918.4 ± 175.6 fl, which is in agreement with 1767.1 fl, the volume of a 15 μm diameter sphere, within the margin of error. The margin of error of volume measurement by this method was 9.2%. We experimentally determined the contribution of errors: The inaccuracy of focus z-position contributes approximately 1-2%, the uncertainty of refractive index approximately 4%, and the uncertainty of image segmentation approximately 6%.

To apply the refractive index contrast method to live cells, the refractive index contrast agent needs to meet two requirements. It should not enter the inside of the cell and should not increase osmotic pressure of the media so that the volume of the cell does not change. We find that high molecular weight polysaccharides such as Ficoll or colloidal silica particles like Percoll are excellent refractive index contrast agents for live cell volumetry. We performed volume measurements of dissociated mouse tibia chondrocytes by increasing the refractive index of the media using 3% Ficoll. This measurement requires dissociated chondrocytes to remain in the same position after changing the media. To increase adhesion, we plated and incubated dissociated chondrocytes on glass bottom dishes coated with Concanavalin A as in Mattes, et. al[40]. Dissociated cells were imaged in DMEM/F12 and again immediately after media change to DMEM/F12 with 3% Ficoll. Although we found that the largest cells do not adhere to the coated glass coverslip, cells with a volume up to about 9,300 fl and thus late in the phase of dry mass dilution could be measured. The refractive index of media and Ficoll containing media was measured to 4 decimal places using Abbe refractometer in each experiment. The difference of the refractive index was typically 0.004. The volume measured using Eq. 7 is compared with the sphere volume calculated from the cells' diameter in Fig. S13a. The volume measured using the refractive index contrast method deviates by 9% from that of perfect spheres. While this is within the margin of error described in the bead experiment, it is possible that the adhesion of cells to the Concanavalin A substrate actually changes the shape of the cells. Nevertheless, the dry mass density measured by DPM and refractive index contrast method also shows the same reduction in the large cells (Fig. S13b). Neither the 9% deviation from sphericity nor the 9.2% measurement uncertainty, as measured with beads, are sufficient to explain the 60% dilution of dry mass density.

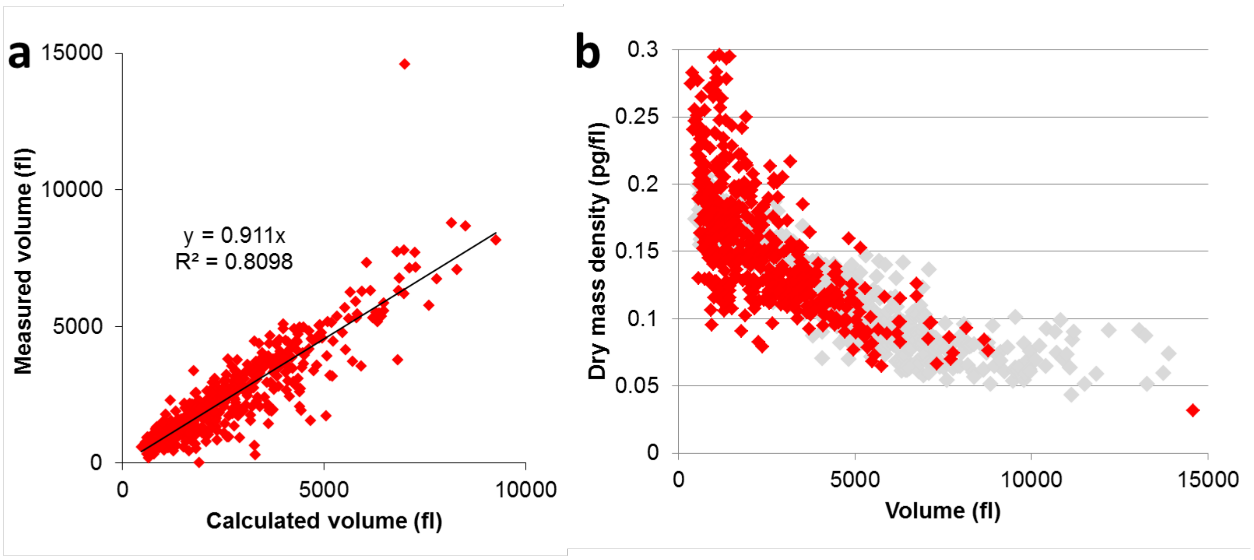

Figure S13: Refractive index contrast method of measuring cell volume is in agreement with the assumption that dissociated chondrocytes assume a spherical shape. (**a**) Volumes measured using refractive index contrast method versus the volumes of the same cells calculated by assuming spherical shape (N=513). (**b**) Dry mass density versus volume plot based on volumes measured by refractive index contrast method (red) follows the same trend as the plot obtained from sphericity assumption (grey).

Regularized Tomographic Phase Microscopy

Regularized tomographic phase microscopy (RTPM) enables a direct assessment of the three-dimensional refractive index map of live cells, and thereby provides cell dry mass density and volume information[41]. RTPM collects quantitative phase images at multiple angles of illumination onto the sample, and reconstructs the 3-D refractive index map utilizing an iterative algorithm providing high resolution and accuracy despite limited angular coverage of the illumination. For data collection, we use a He-Ne laser (λ = 633 nm) as the illumination source, and vary the illumination direction using a galvanometer scanner (DGM, Model 6650, Cambridge Technology) installed at the back focal plane of the condenser lens[42,43]. At each angle of illumination, a quantitative phase image is obtained using an off-axis digital holography based on Mach-Zehnder interferometry. For each tomogram, 400 raw interferograms are acquired at 3000 frames/sec using a complementary metal oxide semiconductor (CMOS) camera (1024PCI, Photron) synchronized with the galvanometer scanner. Using a high-NA condenser lens (1.4NA, Nikon), the maximum angular coverage of 60° can be achieved with respect to the optical axis. The remaining data corresponding to the angle from 60° to 90° can be restored by the regularization algorithm using *a-priori* knowledge about the sample. In a recent numerical simulation, the spatial resolution of RTPM was found to be diffraction-limited along all three axes, and the accuracy of refractive index prediction to be within 0.001[44].

The 3-D distribution of dry mass density was obtained from the 3-D refractive index map by applying Eq. 2. The total dry mass of each cell was calculated from the volume integral of the 3-D distribution of dry mass density. The average dry mass density of each cell was calculated by spatially averaging the dry mass density distribution within the boundary of the cell where the boundary was determined by thresholding the refractive index map. The volume of each cell was calculated by dividing total dry mass by the average dry mass density. Fig. 1e-f and S14b-c show the horizontal and vertical cross sections of two representative cells. The smaller cell's average refractive index is 1.369 while that of the large cell is 1.349, corresponding to 0.180 pg/fl and 0.064 pg/fl of dry mass concentration respectively. The dry mass density as a function of cell volume is shown in Fig. S14a. The absolute values of the concentration and the three phases of density change are in agreement with DPM measurement including an approximate 60% reduction in dry mass density.

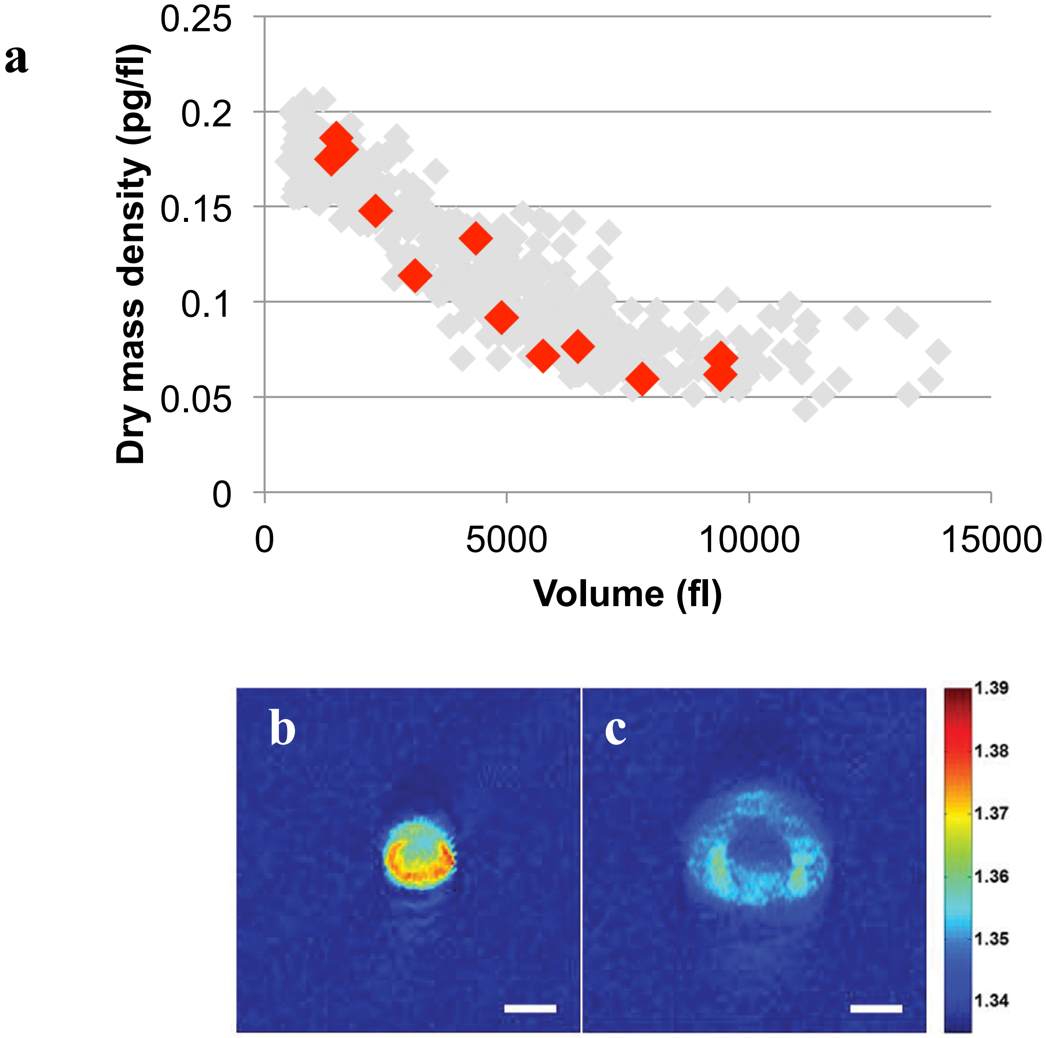

Figure S14: (a) Dry mass density measured by RTPM (red) is in agreement with the dry mass density measured by DPM with spherical assumption (gray). Vertical cross sections of a small (b) and large (c) mouse chondrocyte.

Statistical analysis

To quantitatively compare the size distributions of different cell populations, we applied the rank sum test using Matlab. The rank sum test is a statistical hypothesis test that estimates the probability of the null hypothesis that two data sets are independent samples from the same distribution. Table 1 shows the p-values of the rank sum test of each pair of populations shown in the upper row and left column. We find that the size distribution of mouse tibia cells is different from that of mouse metatarsal cells (p<0.01). In contrast to mouse, the size distribution of metatarsal cells and tibia cells are similar (p=0.59) in jerboa. Any mouse cell type is different from any jerboa cell type (p<0.01).

	mouse tibia	mouse metatarsal	jerboa tibia	jerboa metatarsal
mouse tibia	1	1.54E-04	1.82E-58	2.25E-60
mouse metatarsal		1	6.76E-79	2.10E-74
jerboa tibia			1	0.5937
jerboa metatarsal				1

Table 1. P-value of rank sum test of pairs of cell populations.

Supplemental References

24. Jordan, B., Vercammen, P. & Cooper, K. L. Husbandry and breeding of the lesser Egyptian Jerboa, Jaculus jaculus. *Cold Spring Harb Protoc* **2011**, 1457–1461 (2011).
25. Maroudas, A. & Evans, H. A Study of Ionic Equilibria in Cartilage. *Connective Tissue Research* **1**, 69–77 (1972).
26. Urban, J. P. G., Hall, A. C. & Gehl, K. A. Regulation of matrix synthesis rates by the ionic and osmotic environment of articular chondrocytes. *Journal of Cellular Physiology* **154**, 262–270 (1993).
27. Errington, R. J., Fricker, M. D., Wood, J. L., Hall, A. C. & White, N. S. Four-dimensional imaging of living chondrocytes in cartilage using confocal microscopy: a pragmatic approach. *Am. J. Physiol.* **272**, C1040–1051 (1997).
28. Lecine, P., Blank, V. & Shivdasani, R. Characterization of the hematopoietic transcription factor NF-E2 in primary murine megakaryocytes. *J. Biol. Chem.* **273**, 7572–7578 (1998).
29. Shivdasani, R. A. & Schulze, H. Culture, Expansion, and Differentiation of Murine Megakaryocytes. doi:10.1002/0471142735.im22f06s67
30. Popescu, G. *et al.* Fourier phase microscopy for investigation of biological structures and dynamics. *Opt Lett* **29**, 2503–2505 (2004).
31. Barty, A., Nugent, K. A., Paganin, D. & Roberts, A. Quantitative optical phase microscopy. *Opt. Lett.* **23**, 817–819 (1998).
32. Marquet, P. *et al.* Digital holographic microscopy: a noninvasive contrast imaging technique allowing quantitative visualization of living cells with subwavelength axial accuracy. *Opt. Lett.* **30**, 468–470 (2005).
33. Carl, D., Kemper, B., Wernicke, G. & Von Bally, G. Parameter-optimized digital holographic microscope for high-resolution living-cell analysis. *Appl. Optics* **43**, 6536–6544 (2004).
34. Saleh, B. E. A. *Fundamentals of Photonics*. (Wiley-Interscience, 2007).
35. Barer, R., Ross, K. F. A. & Tkaczyk, S. Refractometry of Living Cells. *Nature* **171**, 720–724 (1953).
36. Zhao, H., Brown, P. H. & Schuck, P. On the Distribution of Protein Refractive Index Increments. *Biophysical Journal* **100**, 2309–2317 (2011).
37. Kujawinska, M. & Wojiak, J. Spatial phase-shifting techniques of fringe pattern analysis in photomechanics. *Society of Photo-Optical Instrumentation Engineers (SPIE) Conference Series* **1554**, 503 (1991).
38. Oh, S. *et al.* Label-free imaging of membrane potential using membrane electromotility. *Biophys. J.* **103**, 11–18 (2012).
39. Visser, T. D. & Oud, J. L. Volume measurements in three-dimensional microscopy. *Scanning* **16**, 198–200 (1994).
40. Mattes, M. J., Tanimoto, M., Pollack, M. S. & Maurer, D. H. Preparing monolayers of non-adherent mammalian cells. *J. Immunol. Methods* **61**, 145–150 (1983).
41. Sung, Y., Choi, W., Lue, N., Dasari, R. R. & Yaqoob, Z. Stain-free quantification of chromosomes in live cells. *PLoS ONE* **7**, e49502 (2012).
42. Choi, W. *et al.* Tomographic phase microscopy. *Nat Meth* **4**, 717–719 (2007).
43. Sung, Y. *et al.* Optical diffraction tomography for high resolution live cell imaging. *Opt. Express* **17**, 266–277 (2009).

44. Sung, Y. & Dasari, R. R. Deterministic regularization of three-dimensional optical diffraction tomography. *J. Opt. Soc. Am. A-Opt. Image Sci. Vis.* **28**, 1554–1561 (2011).